13.8 kV Operation of a Peak-Shaving Energy Storage Equipment With Voltage Harmonics Compensation Feature

WILSON C. SANT'ANA[1], (Member, IEEE), **DENIS MOLLICA**[2],
GERMANO LAMBERT-TORRES[1], (Fellow, IEEE), **BRUNO P. B. GUIMARAES**[3],
GUILHERME G. PINHEIRO[3], **ERIK L. BONALDI**[1], **RONDINELI R. PEREIRA**[3], (Member, IEEE),
LUIZ EDUARDO BORGES-DA-SILVA[3], (Senior Member, IEEE), **ROBSON BAUWELZ GONZATTI**[3],
(Member, IEEE), AND JOSELINO SANTANA-FILHO[2]

[1]Departamento de Pesquisa e Desenvolvimento, Instituto Gnarus, Itajuba 37500-052, Brazil
[2]Departamento de Engenharia, EDP Sao Paulo Distribuicao de Energia, Sao Paulo 08820-460, Brazil
[3]Instituto de Engenharia de Sistemas e Tecnologia da Informacao, Universidade Federal de Itajuba, Itajuba 37500-903, Brazil

Corresponding author: Wilson C. Sant'ana (wilson_santana@ieee.org)

ABSTRACT This paper presents the development and operation on 13.8kV distribution systems of a peak-shaving equipment with battery energy storage. This equipment injects active power to grid during peak times (when the cost of energy is higher) and charges its battery banks from the grid at the off-peak times (when the energy has a low producing cost). The equipment is based on a multilevel converter coupled to the grid through a 2.4kV:13.8kV transformer. In addition to the peak-shaving functionality, a feature of compensation of harmonics on the distribution voltage is included, without the need for any extra sensor nor hardware (apart from the ones already in use for the peak-shaving). The compensation of voltage harmonics is performed through the emulation of a harmonic resistance in order to damp resonances between system impedances that are excited by non-linear loads. This approach is very appealing to distribution systems, where the non-linear loads are not accessible and are scattered. Experimental results obtained on a 13.8kV test substation are presented.

INDEX TERMS Batteries, energy storage, power harmonic filters, multilevel converters.

I. INTRODUCTION

The inevitable exhaustion of recoverable fossil fuels can be roughly estimated by around the end of this century [1]. This fact and also the negative environmental impact of fossil fuels have motivated an increasing usage of renewable energy sources [2]. However, the intermittent nature of these renewable sources has introduced issues of system stability, reliability and power quality [3]. In order to address the intermittency issues, it is necessary to match the intermittent power generation with load demand - which can be achieved with energy storage systems, as they are capable to equalize fluctuations and compensate the mismatch between generation and consumption [4].

The mismatch between generation and consumption is also an issue regarding traditional steady output generation and a load profile that drastically changes during periods of the day or seasons of the year. In order to properly supply the peaks in demand, the whole system must be designed with a capacity over its nominal - which implies in the system operating on its limits during some periods of the day and well bellow its maximum capacity on other periods [5]. In theses cases, also, an energy storage system, would greatly increase the overall efficiency by storing energy during low demand periods and injecting this energy back to the grid during the peak times - in an application known as Peak-Shaving.

The decision on the storage of energy or its injection back to the grid can be of deterministic nature (where fixed time-of-the-day are used for storage and injection, such as presented in [6]) or of probabilistic/stochastic nature (where the demand is forecast considering uncertainties, such as presented in [7]). Most of the time, this decision can be supported with the use of software tools that can simulate and plan the integration of renewable sources. A review

The associate editor coordinating the review of this manuscript and approving it for publication was Bernardo Tellini.

of 37 of the most popular of such softwares tools is presented in [8].

Electrical energy can be stored by means of its conversion into another form of energy and, then, reused by the reverse process. Comprehensive reviews on energy storage system are presented in [2] and [9] - here these systems are only superficially grasped. When the electrical energy is converted into mechanical energy, the three most utilized systems are Pumped Hydro Storage (PHS) [10], where water is pumped from a lower to an upper reservoir (hence with higher potential energy); Compressed Air Energy Storage (CAES) [11], where a gas under pressure is compressed into a reservoir (to be later expanded and move a turbine in order to generate electricity); Flywheel Energy Storage (FES) [12], where a massive spinning cylinder stores the kinetic energy from a reversible electric machine (motor/generator). Electrical energy can also be converted into electrochemical energy and stored in batteries (either of conventional chemistries or of the more innovative flow technologies) [13]. Also, hydrogen fuel cells [14] provide a clean storage solution, as the energy is stored in the hydrogen (through the electrolysis of water - producing oxygen as a by-product), that is later recombined recombined with the oxygen, producing energy and releasing only water vapor in the environment [2]. Finally, the electrical energy can also be stored directly, either on the electric field of a supercapacitor [15] or on the magnetic field of a Super Magnetic Energy Storage (SMES) [16].

Each of the referred storage alternatives is more suitable to a given application than others, depending on power and energy ratings, response time, weight, volume and operating temperature [3]. According with [17], CAES, PHS and batteries are more suitable to applications requiring high energy density (constant power for long periods of time - from minutes to hours), whereas SMES, supercapacitors and flywheels are more suitable for applications requiring high power density (bursts of high power for short periods of time - from few seconds to some minutes). Considering a Peak-Shaving application, where the storage system must be able to supply power for some hours, CAES and PHS would be the most appropriate solutions for massive storage [1] - however as they both require costly infrastructure (and also special site requirements), for smaller power ratings, the storage on batteries becomes the best option.

In a recent paper [18], the authors have presented some preliminary results of a peak-shaving experiment with lead-acid battery storage. In that paper, the experimental results had been obtained in a single-phase 127V test bench. Here, an extension of that paper is proposed, presenting the results and implementation details for the equipment's operation in a three-phase 13.8kV test substation. The greatest challenge concerning the 13.8kV operation is the blocking voltage capability of the semiconductors used in the electronic converter. In [19], the authors have used a distribution transformer to increase the voltage capability of a series active power filter. However, the higher the transform ratio, the higher will be the current ratings at the low voltage side.

Here, a transformer is still used - however, using a multi-level topology on the converter, the transform ratio can be decreased and also the current rating of the semiconductors.

Although the literature presents algorithms based on real time monitoring of demand [20] and stochastic predictions of the demand [7], this present paper takes the more simple and deterministic approach, using a fixed known time table in order to decide about the power injection. Although simple, this approach is perfectly valid when the demand profile is known, as in the case of the Brazilian residential consumers (as reported in [21]). And, considering an intention of this paper to serve as a didactic reference material (the underlying project from which this paper originates is a partnership between an university, a research institution and a utility company), a fixed time table of operation is the best solution in order to explicitly show the different stages of operation of the equipment - although its power reference command could be easily switched to a more complex stochastic approach.

Another aspect that this paper presents is the damping of harmonic propagation on distribution networks (in order to improve voltage quality). Harmonic propagation is the result of series and/or parallel harmonic resonance between line inductors and shunt capacitors installed on the distribution system [22]. Traditional Active Power Filters (APF) (which also comprise STATCOMs and UPQCs [23]) have been successfully employed to mitigate harmonic distortion since decades. However, for optimal use, previous knowledge of the type of load, either being of current source type (rectifiers with large DC inductance) or voltage source type (rectifiers with large DC capacitance) is required [24]. Moreover, according with [22], there are unidentified loads (low power loads that produce a negligible amount of distortion when considered individually - however several of them may cause large distortion to the system). Also, traditional APFs must be installed in the vicinity of the loads that one desires to compensate. However, in a distribution line, as the number of non linear loads might be high and, as these loads might be scattered along the line, the use of one dedicated APF to each non linear loads would not be economically viable. Hence, it is proposed in [22] the use of only one shunt APF to mitigate harmonic propagation on the entire line - instead of the direct compensation of the distorted currents. The basis for using a shunt APF in order to damp resonances, actually, has been introduced in [25]. In that work, the goal was to damp resonances between the grid impedance and the impedance of passive filters and capacitor banks. According with [25], the use of a passive resistance in order to damp the resonances would increase losses. On the other hand, the use of an emulated harmonic resistance can damp the harmonic components without having an influence on the fundamental frequency - hence without dissipative losses. As the APF must emulate a harmonic resistance, this application is known as Resistive Active Power Filter (RAPF).

This approach of damping resonances / harmonic propagation (instead of the conventional local compensation of non-linear loads) is very attractive to be used as an

additional feature to the peak-shaving equipment, as no extra sensors nor additional hardware investment is required. The damping of harmonic propagation functionality has been added by the authors in [26] as a feature to a peak-shaving application (without the necessity of any extra sensors nor additional hardware - other than the ones already used in the peak-shaving application). However, that paper has been written in Portuguese language - which restricts its usage to only a fraction of the readers. Moreover, just like in [18], in [26] the results have also been collected in a 127V test bench. Here the same idea is extended to 13.8kV distribution level. It is important to note that a harmonic damping compensation has already been proposed as a feature in inverter-interfaced distributed generators in references [27]–[29]. In this current paper, a similar feature is proposed for a peak-shaving equipment.

Section II presents the theory of operation of the peak-shaving equipment and its control algorithms. In Section III the added feature of damping of harmonic propagation is presented in detail. Section IV presents the hardware aspects of the developed equipment, including the solutions to some practical issues. Experimental results in a 13.8kV test substation are presented in Section V.

II. PEAK-SHAVING

Figure 1 presents the three-phase electrical circuit of the peak-shaving equipment. It is composed by the connection of three single-phase independent modules connected through a coupling transformer. Each of these single-phase modules is a cascaded H bridge multilevel converter (although other topologies could have been used as well) described in subsection II-A. The control of each of the single-phase modules is based on reference [18] and is overviewed in Figure 2.
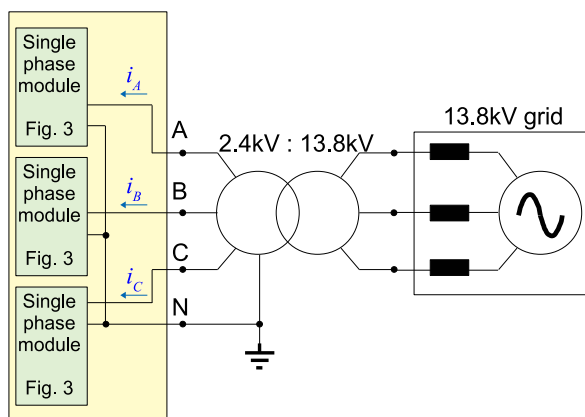

FIGURE 1. Electrical circuit of the three-phase peak-shaving equipment.

The *Decision on AC Power & Battery Control* block (described in subsection II-B) determines the reference value for amplitude of the AC current $i_\Phi{}^*$ (where Φ can be any of the three phases A, B or C). This amplitude can have a positive or negative value (depending if the equipment is injecting power to the grid or charging the battery banks from the grid) and is multiplied by an unitary sinusoid (obtained
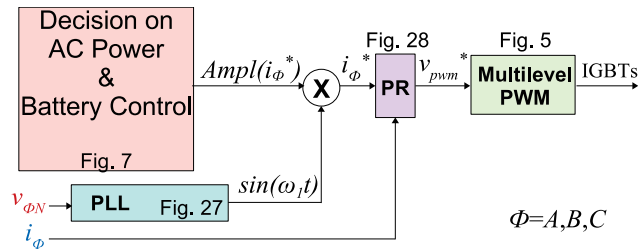

FIGURE 2. Overview of the peak-shaving functionality.

from a digital *PLL*. The appendix A presents the implementation details of the *PLL*. It is important to note that any of the popular *PLL* schemes presented in the review [30] could have been used. From these, the method of [31] has been chosen, as it does not require the tuning of a PI controller. The unitary sinusoid is always in phase with the installation site line-neutral voltage $v_{\Phi N}$. Hence a positive amplitude results in an AC current in phase with the AC voltage and a negative amplitude results in an AC current 180° out of phase with the AC voltage.

The actual AC current i_Φ, generated by the converter, must track its reference with zero error - thus a closed loop controller is used. However, it is important to note that traditional *PI* (Proportional plus Integral) controllers are not able to track sinusoidal references without steady-state errors. Hence, a *PR* (Proportional plus Resonant) controller is used (whose implementation details are presented in the appendix B).

The output of the *PR* controller $v_{pwm\Phi}{}^*$ is the reference for the multilevel *PWM* modulator described in subsection II-A.

A. MULTILEVEL CONVERTER AND PWM MODULATOR
Reference [32] presents a comprehensive review on converter topologies applied to battery energy storage systems. Some of these topologies rely on transformers to elevate the converter output voltage from hundreds of volts to medium voltage levels (at the order of tens of kVs). However, the higher the transform ratio, the higher will be the current that the semiconductors will have to support. In order to avoid the bulky, lossy and costly transformers, [32] also presents multilevel topologies based on series connection of submodules.

A review on multilevel converters for grid interface is presented in [33]. Among them, the Cascaded H-Bridge (CHB) topology (presented in Figure 3) has been chosen, as it is a modular topology and each submodule is the well known H bridge (also known as full bridge) converter. The submodules are connected in series from their AC terminals, which results in isolated DC terminals at each submodule - which, in turn, makes this topology ideal for systems fed with batteries.

Regarding PWM methods for the CHB topology, section 7.4 of [34] discusses about two techniques:

- phase-shift PWM: where the triangular carriers have the same frequency and amplitude, but have a phase shift from each other;
- level-shift PWM: where the triangular carriers have the same frequency but are level shifted, vertically
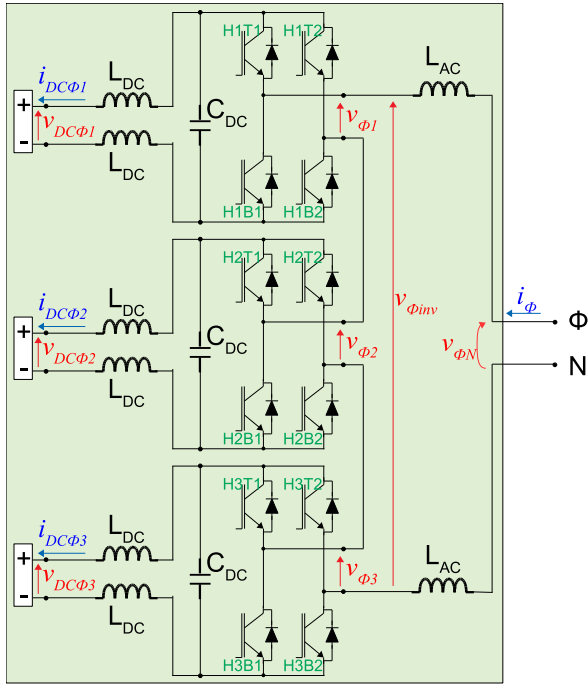
FIGURE 3. Electrical circuit of each of the three single-phase CHB converters of Figure 1.

FIGURE 4. Seven level pattern obtained from three unipolar H bridges.
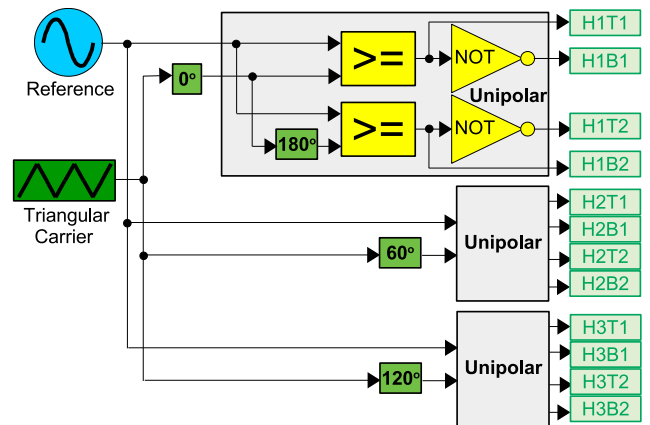
FIGURE 5. Generation of multilevel PWM pulses.

(as opposed to the horizontal displacement of phase-shift carriers).

According with section 7.4 of [34], the level-shift method presents a better THD (Total Harmonic Distortion) than the phase-shift, however the switchings of power semiconductors are uneven among the bridges (which implies in uneven power losses and stresses) and requires some form of power balance strategy. Hence, the phase-shift method has been chosen, due to the fact that it has, intrinsically, equal distribution of power and semiconductor stresses among the bridges [35] and, also, due to its easy programing on DSPs.

Considering that each of the H-bridge submodules operates with an unipolar pattern [36, pp. 215-218] (switching only between one pole at a time: between $+v_{DC}$ and 0V and between 0V and $-v_{DC}$, as seen on the three upper plots of Figure 4), the number m of voltage levels at the resulting series output is given by (1), according with [34, p. 124]. Hence, for the three cascaded H-bridges of Figure 3, the resulting number of voltages levels at $v_{inv\Phi}$ equals seven: $+3 \cdot v_{DC}$, $+2 \cdot v_{DC}$, $+1 \cdot v_{DC}$, 0V, $-1 \cdot v_{DC}$, $-2 \cdot v_{DC}$ and $-3 \cdot v_{DC}$, as seen on the bottom plot of Figure 4.

$$m = 2 \cdot H + 1, \tag{1}$$

where H is the number of series cascaded H bridges.

The resulting staircase pattern presented at the bottom plot of Figure 4 originates from the intentional phase shift inserted between the triangular carriers of each of the submodules during the generation of PWM pulses. The phase shift ϕ_{cr} among each PWM carrier is given by (2), according with [34, p. 127]. Hence, for the three cascaded H-bridges of Figure 3, the phase shift must be 60° - which results in
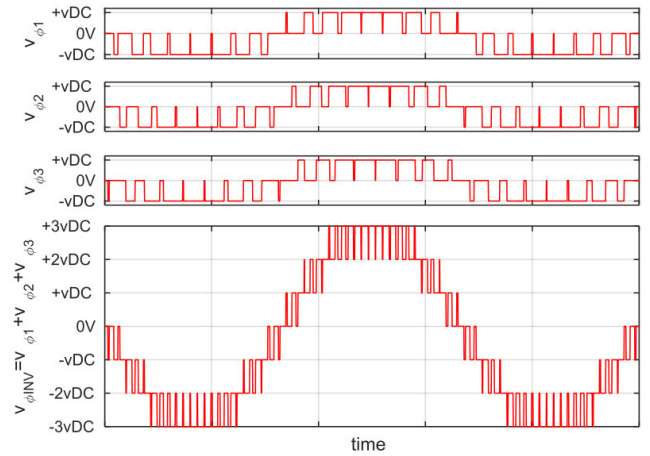
the relative angle of the triangular carriers as 0° (and its complimentary 180°), 60° (and its complimentary 240°) and 120° (and its complimentary 300°). Figure 5 presents a block diagram of the multilevel modulator for three H-bridges. It can be noticed that the well know structure of the unipolar PWM [36, pp. 215-218] is repeated three times - whereas the only difference between them is the phase angle of the triangular carrier. A detailed procedure for programming the PWM modules of the TMS320F28335 DSP aiming multilevel converters is presented in [37]. Also this procedure must be similar for other devices within the C2000 family of Texas Instruments DSPs.

$$\phi_{cr} = \frac{360°}{m-1} = \frac{360°}{H}. \tag{2}$$

B. DECISION ON THE AC POWER AND BATTERY CONTROL

Figure 6 presents the proposed discharge profile of the batteries, based on a known demand. Four time marks (t_1, t_2, t_3 and t_4) are specified, where the reference for the DC current $i_{DC\Phi}{}^*$ varies according to the position of the time of the day in relation to theses time marks.

During the peak time interval (from t_2 until t_3), the DC current discharge is maximum, with value I_{DCmax}.

However, there is a time interval before the peak (from t_1 until t_2) where the demand is still growing - hence the DC current follows an increasing ramp (negatively) according with (3). Following the same reasoning, there is a time interval after the peak (from t_3 until t_4) where the demand is decreasing - hence the DC current follows a decreasing ramp (negatively) according with (4). Then, after t_4, the converter starts to recharge the batteries - preparing them for the next injection cycle at the next day.

$$i_{DC\Phi}^*\big|_{increasing} = I_{DCmax} \cdot \frac{t - t_1}{t_2 - t_1}. \tag{3}$$

$$i_{DC\Phi}^*\big|_{decreasing} = I_{DCmax} \cdot \left(1 - \frac{t - t_3}{t_4 - t_3}\right). \tag{4}$$

Both the discharging and recharging of the batteries take place indirectly, as the AC current is controlled by the PR controller. According with the signal convention of Figures 1 and 3, for an AC current in phase with the AC voltage, the power flows from the grid to the batteries (thus recharging them) with a positive average value on the DC currents. The amplitude of i_Φ (in phase with $v_{\Phi N}$) determines how positive is the average value of $i_{DC\Phi H}$ (where the H index refers to any of the H bridges in Figure 3).

Conversely, for an AC current 180° out of phase with the AC voltage, the power flows from the batteries to the grid with a negative average value on the DC currents. The amplitude of i_Φ (180° out of phase with v_Φ) determines how negative is the average value of $i_{DC\Phi H}$.

According with Figure 6, the knowledge of the time of the day (t) is crucial to whether recharge the equipment batteries or to inject power to grid (and in what amount of injection). To accomplish this, a real-time-clock from a GPS module has been used. This module communicates with the DSP via serial UART protocol. A detailed procedure for UART communication between the TMS320F28335 DSP and the GPS is provided in [18], as well as a procedure to decode the time of the day information from the data received (which also includes several other information).
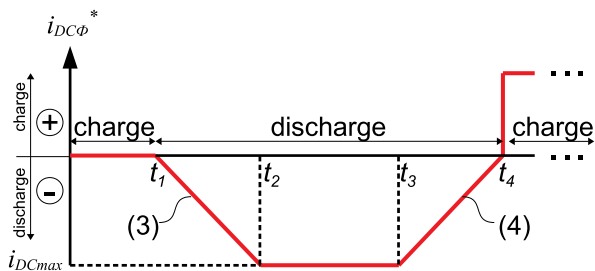
FIGURE 6. Discharge profile for the DC current based on the time of the day.

Figure 7 presents the internal diagram of the *Decision on AC power & Battery Control* block of Figure 2. After, the time of the day information has been received and decoded from the GPS module, the reference for the DC current $i_{DC\Phi}^*$ can be determined based on the flowchart of Figure 8.
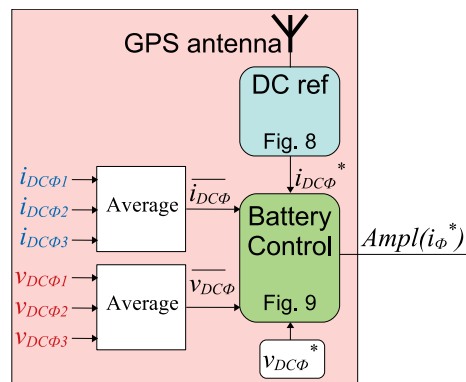
FIGURE 7. Decision on the AC power based on battery measurements and time of the day information.
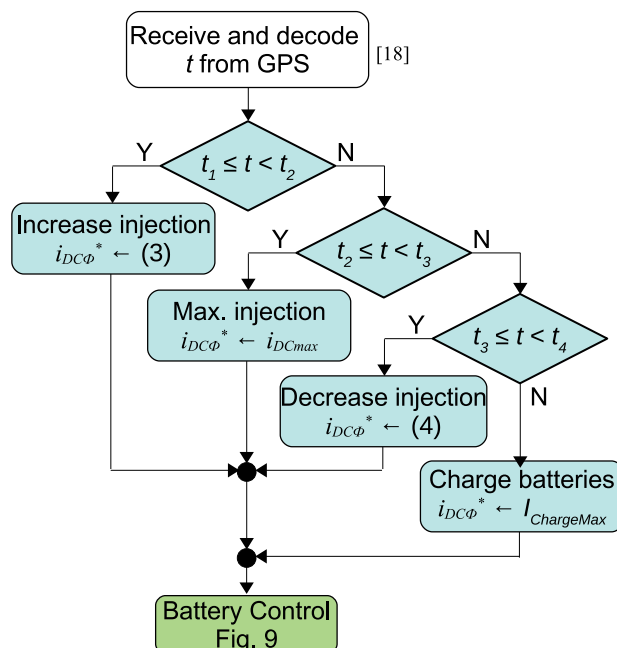
FIGURE 8. Decision on the DC current reference based on the time of the day information.

As informed previously, the DC currents $i_{DC\Phi H}$ are indirectly controlled by the amplitude of the AC current i_Φ, according with the flowchart of Figure 9. Besides the reference for the DC currents $i_{DC\Phi}^*$, this block also has as inputs the average value $\overline{i_{DC\Phi}}$ of the DC currents of all H bridges at the phase Φ ($i_{DC\Phi H}$, for $H = 1, 2, 3$), the average value $\overline{v_{DC\Phi}}$ of the DC voltages of all H bridges at the phase Φ ($v_{DC\Phi H}$, for $H = 1, 2, 3$) and the reference for the DC voltage $v_{DC\Phi}^*$. It is interesting to note that $i_{DC\Phi}^*$ is tracked by $i_{DC\Phi H}$ only during battery discharge and during the stage I of the charging process and that $v_{DC\Phi}^*$ is tracked by $v_{DC\Phi H}$ only during the stages II and III of the charging process.

As described in [38] and illustrated in Figure 10, the charging process of Lead Acid batteries is performed in three stages. During Stage I, the currents in the batteries $i_{DC\Phi H}$ are kept constant (at their reference value $i_{DC\Phi}^*$) while their voltages $v_{DC\Phi H}$ gradually increase (until reaching their
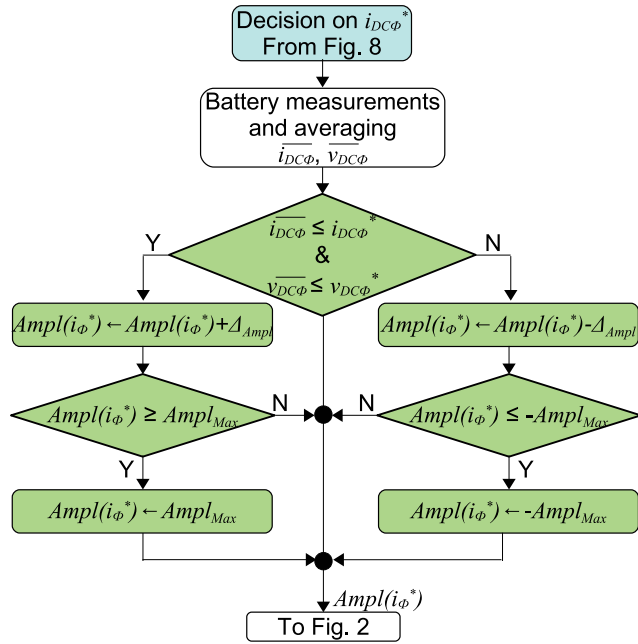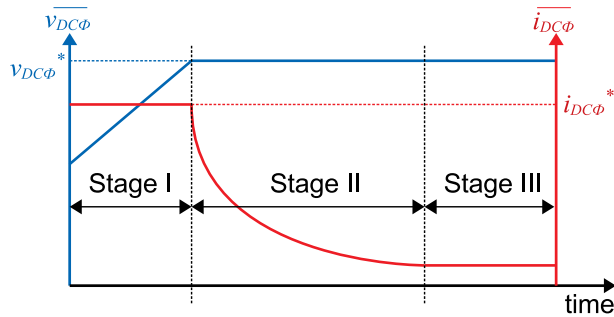
FIGURE 9. Battery control.

FIGURE 10. Charging of lead acid batteries in three stages [38].

reference value $v_{DC\Phi}$*). During Stages II and III, the voltages in the batteries $v_{DC\Phi H}$ are kept constant (at their reference value $v_{DC\Phi}^*$) - however at Stage II the $i_{DC\Phi H}$ slowly drop from $i_{DC\Phi}$* (when they were in Stage I) until near zero (when they pass to Stage III). During Stage III, the batteries are already fully charged and they draw a minimum current only to keep their voltages "floating" around $v_{DC\Phi}$*. The value of the floating voltage is given by the manufacturers. It is possible to adjust this floating voltage in real time in relation to the batteries temperature, in order to preserve their lifetime [39] - however, here, it is considered the manufacturer recommended value at 25°C.

The flowchart of Figure 9 controls the amplitude of the reference AC current i_Φ* by means of its increment/decrement based on the values of $i_{DC\Phi}$*, $\overline{i_{DC\Phi}}$, $v_{DC\Phi}$* and $\overline{v_{DC\Phi}}$. During Stage I charging, the condition $\overline{v_{DC\Phi}} \leq v_{DC\Phi}$* will be always satisfied. Hence, the average value of the DC currents is kept around its reference either by incrementing the amplitude of the AC current ($Ampl(i_\Phi$*)) with a step size Δ_{Ampl} (when $\overline{i_{DC\Phi}} \leq i_{DC\Phi}$*) or by decrementing $Ampl(i_\Phi$*) when $\overline{i_{DC\Phi}} > i_{DC\Phi}$*. On the other hand, during Stages II and III,

the condition $\overline{i_{DC\Phi}} \leq i_{DC\Phi}$* will be always satisfied (as $i_{DC\Phi}$ is a constant maximum charging current and $\overline{i_{DC\Phi}}$ drops as the batteries get charged) and $\overline{v_{DC\Phi}}$ is kept around $v_{DC\Phi}$* either by incrementing or decrementing $Ampl(i_\Phi$*) with a step size Δ_{Ampl}.

Similarly to Stage I charging, when the converter is injecting power from the batteries, the condition $\overline{v_{DC\Phi}} \leq v_{DC\Phi}$* will be always satisfied. However, in this case, the reference for the DC current is negative. Hence $Ampl(i_\Phi$*) is incremented/decremented negatively, in order to achieve an AC current 180° of phase in relation to the AC voltage.

During all three stages of charge and also during discharge, there is a maximum limit for $Ampl(i_\Phi$*), of value $Ampl_{Max}$, which is tested at every increment/decrement.

III. DAMPING OF HARMONIC PROPAGATION

Figure 11 presents the block diagram of the RAPF feature. The damping of harmonic propagation is obtained by the emulation of a harmonic resistance, one for each frequency of interest. From the installation site line-neutral voltage $v_{\Phi N}$, the desired harmonic components are obtained (subsection III-A). Based on these harmonic components, the optimized value for each harmonic resistance is calculated (subsection III-B). For each of the harmonic components of the installation site voltage v_h (where the subscript h refers to a specific harmonic order), a parcel i_h of the total harmonic compensating current i_{harm} is calculated. Finally, i_{harm} is added to the peak-shaving reference current i_Φ* in Figure 2.
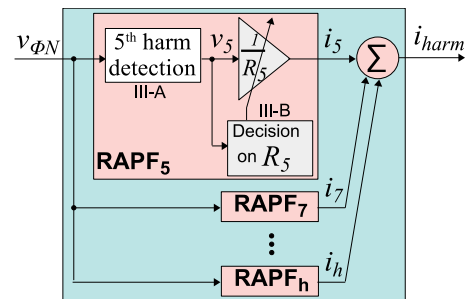

FIGURE 11. Overview of the RAPF feature [26].

A. DETECTION OF VOLTAGE HARMONICS

A survey on methods for harmonic detection is presented in [40]. There are presented time domain and frequency methods, whereas the time domain is more appropriate for real time implementation. However, the majority of these time domain methods requires coordinate transforms, which results in more computational effort. Among the frequency domain methods, it can be highlighted those that introduce high gain and zero phase-shift at a desired frequency by means of a second order transfer function with resonant poles. One of these methods is presented in [41] and is, particularly, interesting for single-phase systems (which is the case of this project, where three independent single-phase systems are connected together). This method, at continuous frequency

domain, is implemented as (5).

$$H_h(s) = \frac{s^2 + \omega_h^2}{s^2 + 2\omega_c s + \omega_h^2}, \tag{5}$$

where ω_h is the tunned frequency and ω_c is the bandwidth of the notch to be generated.

The algorithm of Figure 11 requires one tunned filter for each frequency desired to be damped. Considering the majority of non-linear loads produce distortions at the order of $6 \cdot n \pm 1$ (where $n = 1$, as the superior orders can be considered negligible), it is enough to tune the filters for the 5th and the 7th harmonics - although some other frequencies might be required at specific cases.

As this filter is implemented in a Digital Signal Processor, (5) can be discretized with a Trapezoidal/Tustin method [42], resulting in the difference equation (6). The parameters a_{1vh}, a_{2vh}, b_{0vh}, b_{1vh} and b_{2vh} are obtained as (7).

$$\begin{aligned} v_h^-(t) = &-a_{1vh} \cdot v_h^-(t-1) - a_{2vh} \cdot v_h^-(t-2) \\ &+ b_{0vh} \cdot v_{\Phi N}(t) + b_{1vh} \cdot v_{\Phi N}(t-1) \\ &+ b_{2vh} \cdot v_{\Phi N}(t-2). \end{aligned} \tag{6}$$

$$\begin{cases} a_{0vh} = 4/T_s^2 + 4 \cdot \omega_c/T_s + \omega_h^2 ; \\ a_{1vh} = \left[-8/T_s^2 + 2 \cdot \omega_h^2\right]/a_{0vh} ; \\ a_{2vh} = \left[4/T_s^2 - 4 \cdot \omega_c/T_s + \omega_h^2\right]/a_{0vh} ; \\ b_{0vh} = \left[4/T_s^2 + \omega_h^2\right]/a_{0vh} ; \\ b_{1vh} = a_{1vh} ; \\ b_{2vh} = b_{0vh}, \end{cases} \tag{7}$$

where T_s is the sampling period.

It is important to note that (5) implements a notch filter. Hence, the signal $v_h^-(t)$ contains all frequency components of $v_{\Phi N}(t)$ other than the desired component at order h. Thus, the desired component $v_h(t)$ is obtained as (8).

$$v_h(t) = v_{\Phi N}(t) - v_h^-(t). \tag{8}$$

B. DECISION ON THE HARMONIC RESISTANCE

The harmonic compensating current to be injected into the grid is calculated by the installation site voltage $v_{\Phi N}$ divided by the desired value of harmonic resistance. In general, the lower the resistance value, the better the damping of harmonic propagation - however, the ratings of the APF are required to be higher. The literature indicates several methods to determine an optimal value for the harmonic resistance. In [43] it has been used a distributed parameter model for the distribution line in order to equate the harmonic resistance with the characteristic impedance of the line - however, this value cannot be a fixed value, as there might be connection/disconnection of capacitor banks according with demand. In order to dynamically obtain the characteristic impedance of the line, an ARIMAX parameter estimator is proposed in [44].

The RAPF emulating the characteristic impedance of the line, however, must be installed at the end of a radial line, as they must act as a matching impedance. Other

(and simpler) methods, only vary the harmonic resistance in order to make the harmonic distortion fall bellow a predefined limit. In [45] the THD of the installation site voltage has been compared against a reference value. Whenever the measured THD is higher than its reference, the harmonic resistance is decremented - also, whenever the THD is bellow its reference, the harmonic resistance is incremented. In [46] the harmonic resistance is calculated for each frequency individually, based on the voltage distortion at that frequency, in order to avoid over compensation at the other frequencies.

Figure 12 presents a flowchart to determine the value of the harmonic resistance to be emulated by the RAPF. It is important to note that the same algorithm must be repeated for all desired frequencies - in case of the experimental results presented in section V, the 5th and the 7th harmonics.
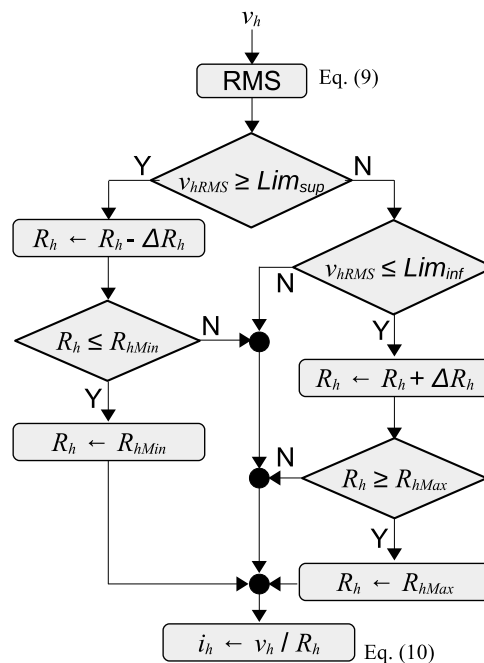
FIGURE 12. Decision on the harmonic resistance and on the compensation current.

The procedure starts with the hth harmonic component of the installation site voltage, obtained in subsection III-A. Then, the RMS value of this harmonic component is calculated as (9).

$$v_{hRMS} = \sqrt{\frac{1}{n_h} \cdot \sum_{k=1}^{n_h} v_{h_k}^2}, \tag{9}$$

where n_h is number of samples in one period of the hth order.

The RMS value of the hth order is compared against a reference value - if superior, then the value of the harmonic resistance R_h is decremented of a value ΔR_h - if inferior, then the value of R_h is incremented. In both cases, a saturation is performed in order to keep R_h between the allowed minimum (R_{hMin}) and maximum (R_{hMax}) values.

Finally, the hth order of the compensation current, which will be responsible to emulate the harmonic resistance R_h at that frequency is calculated as (10).

$$i_h = v_h/R_h. \qquad (10)$$

IV. DEVELOPED EQUIPMENT

Figure 13 presents a photo with a general view of the developed equipment. It is formed by three independent single phase modules, identified as numbers 1, 2 and 3 - whose power circuits have been illustrated in Figure 3. This photo also shows the three battery banks, identified as numbers 4, 5 and 6, one for each phase. Each phase battery bank, in turn, is formed by three floating series array of 67 lead-acid batteries, resulting in $67 \cdot 12V = 804V$ (nominal) for each H-bridge.

FIGURE 13. Photo of the developed equipment (1, 2 and 3) and the battery banks (4, 5 and 6).

Figure 14 presents a photo of the electronics subsystem of one of the three phases. The number 7 identification is the Adafruit GPS board. It communicates with the DSP board (identified as number 8, with a TMS320F28335 processor) via UART (as described in [18]). It should be noted that each phase has its own DSP. This was necessary due to the high number of PWM signals required to control three H-briges per phase.

Number 9 indicated in Figure 14 is a board with 24V relays and optocouplers, required to interface the TTL 3.3V from the GPIOs of the DSP with contactors and the human-machine-interface (buttons and lamps). The input range of the analog signals on the DSP is from 0V to 3V. Hence the output of the CTs and PTs must be conditioned through operational amplifiers (indicated as number 10). Number 11 indicates circuits that translate the TTL 3.3V from the GPIOs to the 15V of the optical fiber interface boards of number 12. From number 12, optical fibers are connected to the H-bridges, in order to command their IGBTs.

Figure 15 presents a photo of the power subsystem of one of the three phases. It should be noted that there are three shelves, on for each H-brige of that phase. The number 13 identifications are the DC capacitors of the H-briges
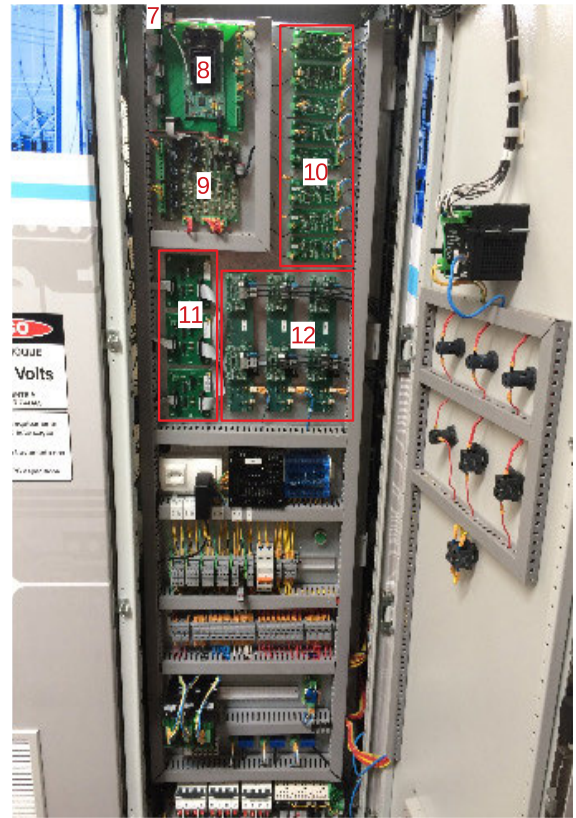

FIGURE 14. Electronics subsystem (of one phase).

while number 14 are the DC inductances (C_{DC} and L_{DC}, respectively, connected as indicated in the circuit of Figure 3). The number 15 identifications are 100W resistances part of the pre-charge circuit of the DC capacitors (described in subsection IV-A).

A. PRE-CHARGING OF THE DC CAPACITORS

Whenever a step voltage variation is applied to a discharged capacitor, the charging current will result in an impulse, proportional to the capacitance value and also on the step variation ($i_C(t) = C \cdot dV/dt$). In case of the developed equipment, due to the high value of the DC capacitors and, mainly, due to the high value of the DC voltages of the battery banks (804V nominal), the impulse on the current, if not properly dissipated, may trip circuit protections or cause damage to some circuit parts.

A pre-charging circuit, through a series resistance (that is short-circuited after the charging time by a contactor) has been proposed in [47]. In that case, there were no battery banks and the capacitor voltage was controlled from the AC current. Here, due to the battery bank connection, the series resistance should be connected on the DC side. Also, in the case of [47], the contactor had to be rated to support the nominal current of the converter. Here a modification is performed, as presented in Figure 16, in order to allow a small rating DC contactor to conduct during the charging time and be released after, for normal operation of the converter.

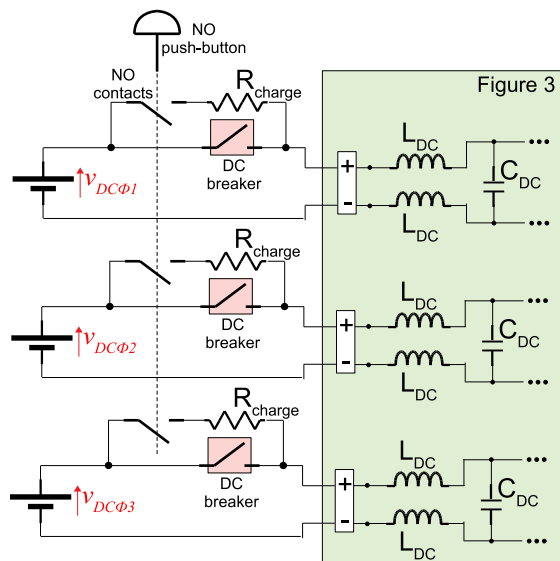**FIGURE 15.** Power subsystem (of one phase).

FIGURE 16. Pre-charging circuit of DC capacitors (of one phase).

Whenever the battery banks must be connected to the equipment, the operator must press the normally open (NO) push-button, commanding a small rating DC contactor (also with NO contacts) to insert the charging resistor (R_{charge} - number 15 in Figure 15) in series with the DC capacitor C_{DC}. The RC time constant formed between R_{charge} and C_{DC} produces a (relatively) slowly rise capacitor voltage - which, in turn, draws a reduced charging current. Once the capacitor

is charged (even, partially charged), the DC breakers can be closed and the equipment is ready to operate. It should be noted that the "slow" rise in the capacitor voltage, actually, correspond to the press and release of the push-button (due to the the fact that the electric dynamics are much faster than the perception of the human operator). Figure 17 presents the waveforms of the voltage (CH1 - yellow) at one of the DC capacitors and its charging current (CH2 - green). It can be noticed that, for $R_{charge} = 100\Omega$ and $C_{DC} = 6666.7\mu F$ (equivalent capacitance of a series-parallel array of $10000\mu F$ capacitors), in less than 2s the voltage reaches its nominal value (804V). It can also be noticed that the peak charging current has been limited by the 100Ω resistance to 8A.
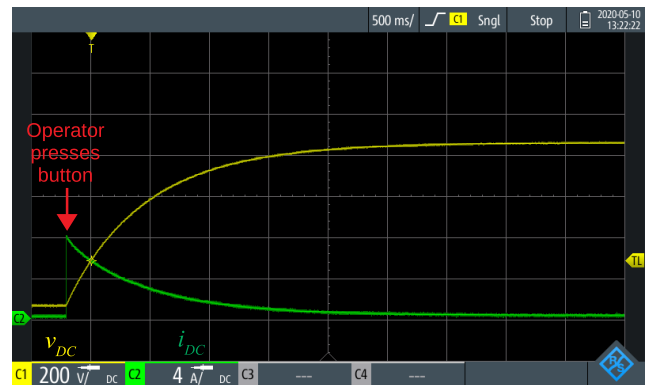

FIGURE 17. Slow pre-charge of DC capacitor using the circuit of Figure 16.

V. EXPERIMENTAL RESULTS

Figure 18 presents the test 13.8 kV substation used in the experiments. The number 16 identification is a 220V:13800V tree-phase transformer used to provide the 13.8kV grid for the tests and number 17 is the 13.8kV:2.4kV coupling transformer of Figure 1. Numbers 18 indicate the PTs and numbers 19 the CTs. The non numbered elements in the photo were not used in the experiments shown in this paper, as this substation is shared with other projects.

Figure 19 presents the operation of the seven level cascaded H-bridge. The yellow plot is the voltage at the output of one of the H-bridges v_{A3}, switching between $+v_{DC}$ and 0V during the positive half cycle and between 0V and $-v_{DC}$ during the negative half cycle. The output of the other two H-bridges at this phase (v_{A2} and v_{A1}) should be similar. The green plot is the resulting voltage at the output of the seven level CHB converter ($v_{Ainv} = v_{A1} + v_{A2} + v_{A3}$). It can be noticed that this green plot is similar to the bottom plot of Figure 4, apart from the ripple at the DC voltage of each H-bridge. The red plot is the AC current i_A of that phase. At this particular instant of operation, the equipment is injecting power to the grid, and the AC current is 180° out of phase in relation the converter output voltage, according with the signal convention adopted in Figure 3.

Two experiments have been performed: the peak-shaving operation (subsection V-A) and the voltage harmonics compensation (subsection V-B).
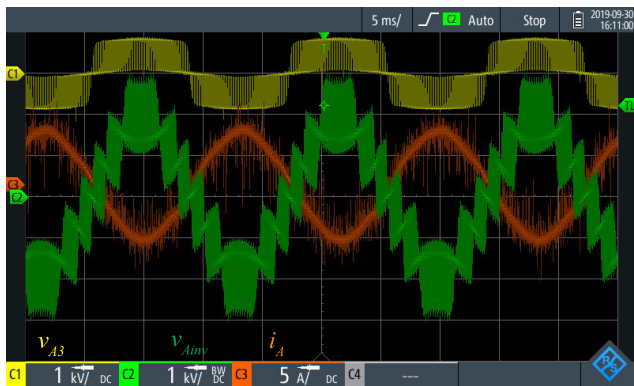
FIGURE 18. Test 13.8 kV substation.

FIGURE 19. Operation of the seven level cascaded H-bridge converter.

A. PEAK-SHAVING OPERATION

In this experiment, a power and energy logger (by Fluke) has been used to acquire the voltages (at the secondaries of PTs) and the currents (at the secondaries of CTs) at the three phases of the 13.8kV buses, in order to obtain a trend of the three-phase power. Also, an oscilloscope (by Rohde & Schwarz), with logger functionality, has been used to obtain the trends of the DC voltage in one of the battery banks and the current at this same bank.

With a sampling interval of 1 minute, during 16 hours (which were enough to show all stages of operation), the aforementioned signals have been acquired, as presented in Figure 20. The trends show the equipment starting power injection to the grid at 13:00 (following the injection profile of Figure 6). From 13:00 until 14:30, the tree-phase power (top plot, black color) increases negatively (according with the signal convention adopted in Figure 3) on a ramp from zero to around -20kW (which was the adopted maximum power for the tests). From 14:30 until 16:30, the equipment is in its maximum (and constant) power injection stage

($P_{max} = -20kW$). From 16:30 until 18:00, the injected three-phase power decreases (negatively) on a ramp from -20kW to zero.

Figure 21 presents the voltages and currents at the 13800V bus (measured at the secondaries of PTs and CTs) at time 15:30 - hence, during maximum power injection into the grid. The upper plots present the three phase-to-ground voltages. The intermediary plots present the three line currents. The lower plots present the voltage and current of a same phase. It can be noticed that the voltage and current are 180° out phase in relation to each other - indicating battery discharge, according with the signal convention adopted in Figure 3.

During the whole injection stage, the monitored battery bank voltage (bottom plot of Figure 20, magenta color) drops from around 890V to around 800V. From 18:00, the battery charging stage starts (consuming a positive power from the grid - according with the signal convention adopted in Figure 3). On this particular test, the stage I of battery charge (constant current - bottom plot, green color) happened from 18:00 until around 22:00, while the battery voltage (magenta) rose linearly until around 890V.

From 22:00 until around 3:00 (of the next day), the batteries were in the stage II of charge - where the batteries voltage (bottom plot of Figure 20, magenta color) are kept constant and their current (bottom plot, green color) slowly drops. From 3:00, the batteries are already in stage III, consuming a minimum power just to keep the floating voltage.

Figure 22 presents the voltages and currents at the 13800V bus (measured at the secondaries of PTs and CTs) just after 18:00 - hence, at the very beginning of stage I charging, when the batteries drain maximum power from the grid. The upper plots present the three phase-to-ground voltages. The intermediary plots present the three line currents. The lower plots present the voltage and current of a same phase. It can be noticed that the voltage and current are in phase in relation to each other - indicating battery charging, according with the signal convention adopted in Figure 3.

B. VOLTAGE HARMONICS COMPENSATION

In this experiment, in order to produce the voltage distortion on the 13.8kV substation, a rectifier of voltage source type (with large DC capacitance) has been installed at the 220V side of the input transformer (number 16 in Figure 18).

Figure 23 presents the trends (obtained with the Fluke Power & Energy Analyzer, sampling at each second) of the three-phase power (top plot) and the voltage distortions (bottom plot - showing the trend of the THD, the 5th and the 7th harmonics). In order to speed up the experiment, the power injection and battery charging profile has been compressed into a 10 minute cycle (instead of 24 hours cycle). In this experiment, two complete cycles are shown: the first one with the harmonic compensation feature ON (from 14:07 until 14:16) and the second one with the harmonic compensation feature OFF (from 14:16 until 14:24).

When the voltage harmonics compensation feature is ON (RAPF ON during the first half of Figure 23), the voltage
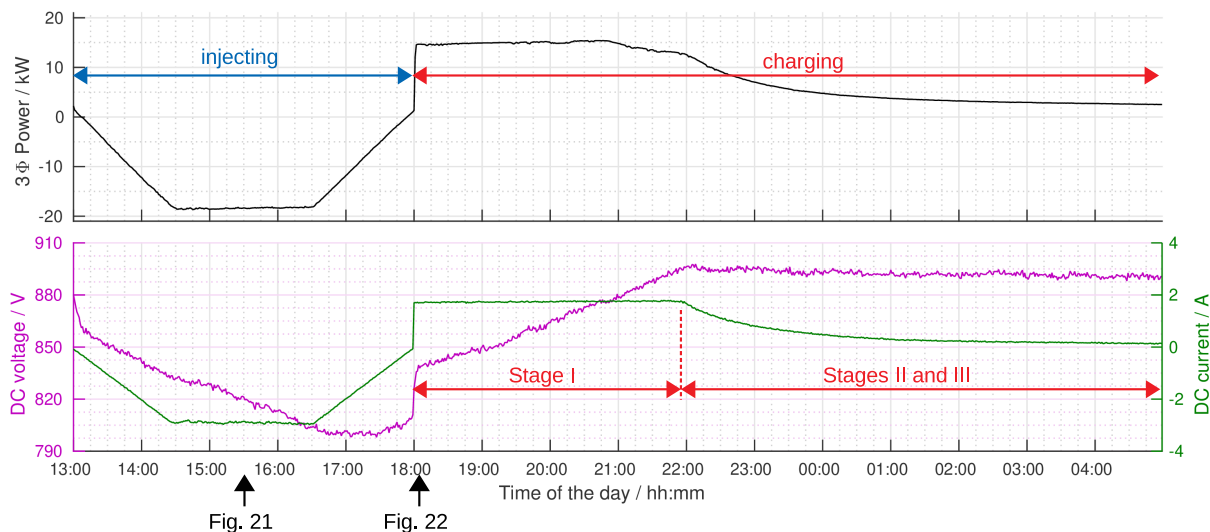
FIGURE 20. Logs of three-phase power at the 13.8 kV side of the transformer and DC voltage and DC current at one of the battery banks, sampled at each minute.
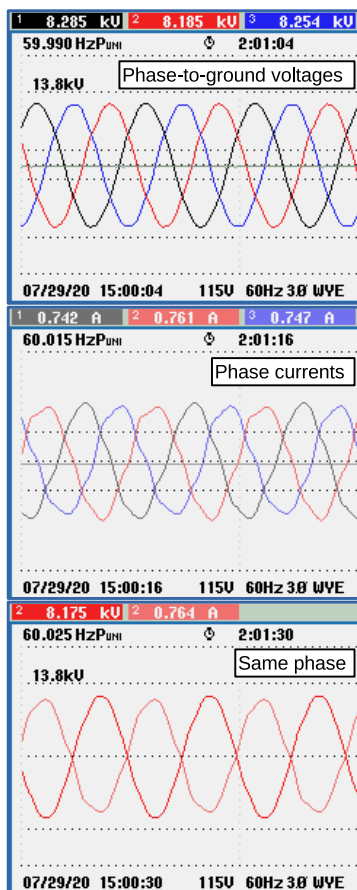

FIGURE 21. Voltages and currents at the 13800V bus during maximum power injection to the grid.
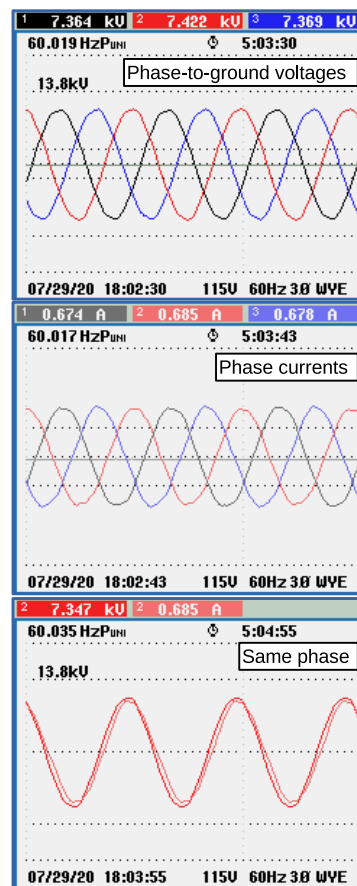

FIGURE 22. Voltages and currents at the 13800V bus during stage I battery charge.

THD has been measured near 1.5% and the individual distortions for the 5th and the 7th have been measured around 0.5%. Then, at t = 14:16, the voltage harmonics compensation

feature is turned OFF (RAPF OFF during the last half of the figure). It can be noticed that the THD has increased from 1.5% to between 4% and 4.5%. The measurement
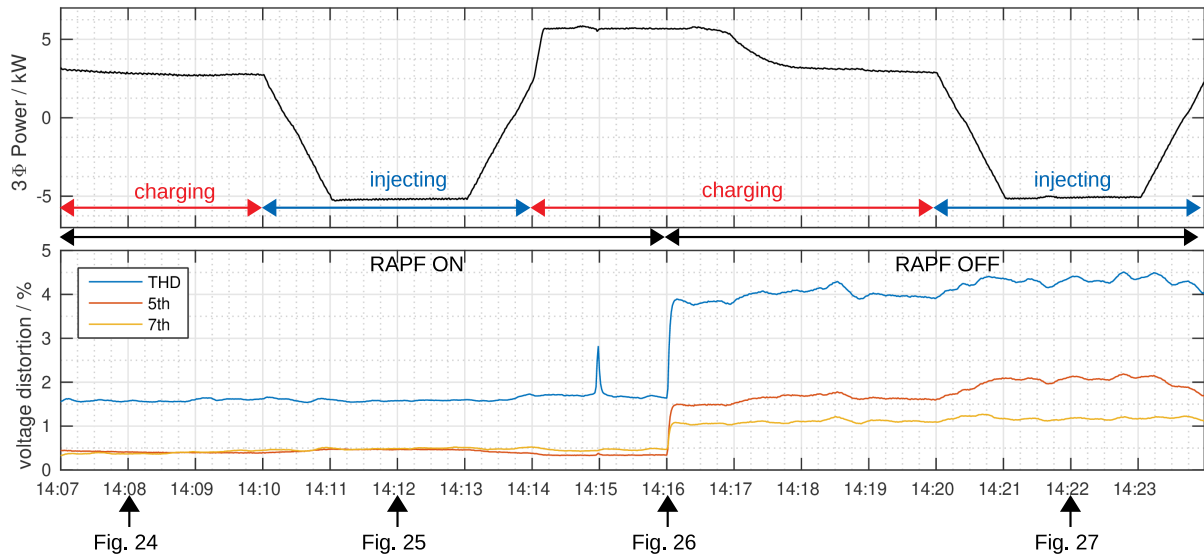
FIGURE 23. Logs of three-phase power and voltage distortions, at the 13.8 kV side of the transformer, sampled at each second.

of the individual 5th harmonic has increased from 0.5% to between 1.5% and 2%. Also, the measurement of the individual 7th harmonic has increased from 0.5% to between 1.0% and 1.3%.

Figures 24 to 27 present the waveforms at each operational stage (with and without harmonic compensation). In these figures, the yellow and the green plots are the AC voltage and AC current (respectively) at the low side of the coupling transformer and the red and blue plots are voltage and current (respectively) in one of the battery banks. The instants of time where each of these measurements were taken have been indicated at the bottom of Figure 23.

Figure 24 presents the measurements taken at t = 14:08, during stage III of battery charging. In this condition, both the AC current (green plot) and DC current (blue plot) are near their minimum values, in order to keep the batteries at their floating voltages. It can be noticed that the AC current is in phase with the AC voltage (yellow plot) and the DC

current has a positive mean value - indicating battery charge, according with the signal convention adopted in Figure 3. It should be noted that the AC current is distorted in order to emulate the harmonic resistance and damp the harmonic distortion on the AC voltage (seen perfectly sinusoidal - with a THD of about 1.5%, as shown in Figure 23).

Still with the harmonic compensation feature turned ON, Figure 25 presents the measurements taken at t = 14:12, during power injection to the grid. In this condition, the AC current (green plot) is 180° out phase in relation to the AC voltage (yellow plot) and the DC current (blue plot) has a negative mean value - indicating battery discharge, according with the signal convention adopted in Figure 3. It should be noted that the AC current is still distorted and the AC voltage is still perfectly sinusoidal (with a THD of about 1.5%, as shown in Figure 23), as the equipment is emulating the harmonic resistance in order to damp voltage distortion.
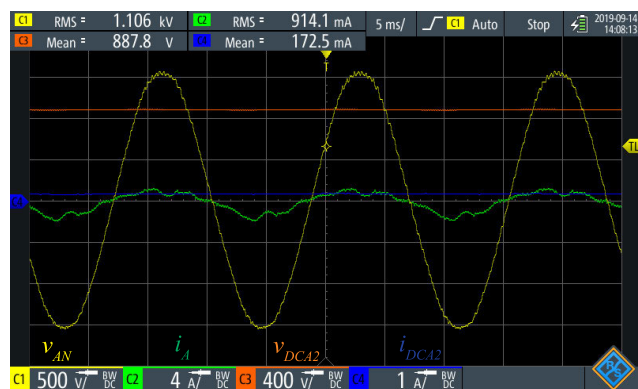

FIGURE 24. Measurements at 14:08, at the 2.42 kV side of the transformer - Converter charging the batteries - with harmonic compensation feature.
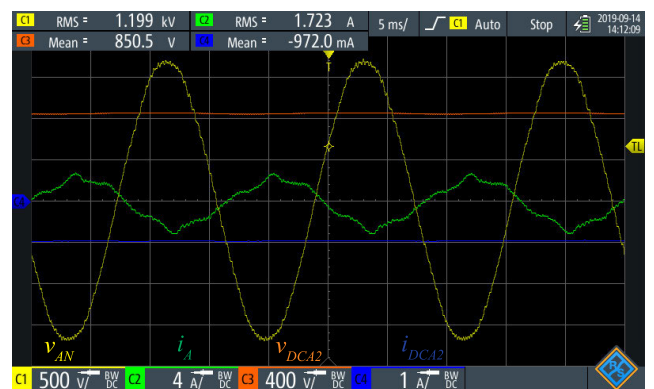

FIGURE 25. Measurements at 14:12, at the 2.42 kV side of the transformer - Converter injecting power into the grid - with harmonic compensation feature.
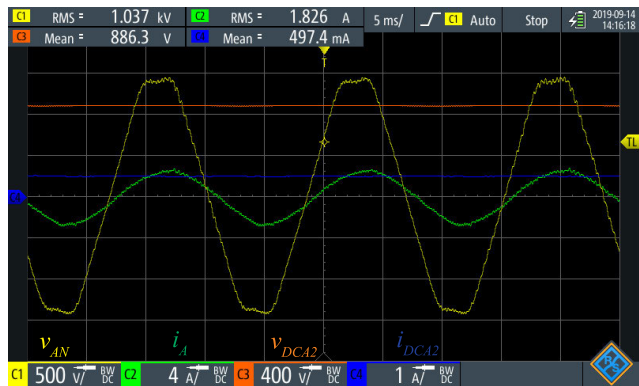
FIGURE 26. Measurements at 14:16, at the 2.42 kV side of the transformer - Converter charging the batteries - without harmonic compensation feature.

Figure 26 presents the measurements taken at t = 14:16, on stage I of battery charging - and with the harmonics compensation turned OFF. In this condition, the AC current (green plot) is in phase in relation to the AC voltage (yellow plot) and the DC current (blue plot) has a positive mean value - indicating battery charge, according with the signal convention adopted in Figure 3. It should be noted that, as the harmonic compensation has been turned OFF, the AC current is sinusoidal and the AC voltage is distorted (with a THD of about 4%, as shown in Figure 23).

Still with the harmonic compensation feature turned OFF, Figure 27 presents the measurements taken at t = 14:22, during power injection to the grid. In this condition, the AC current (green plot) is 180° out phase in relation to the AC voltage (yellow plot) and the DC current (blue plot) has a negative mean value - indicating battery discharge, according with the signal convention adopted in Figure 3. It should be noted that the AC current is still sinusoidal and the AC voltage is still distorted (with a THD of about 4.5%, as shown in Figure 23), as the equipment is no longer emulating the harmonic resistance.
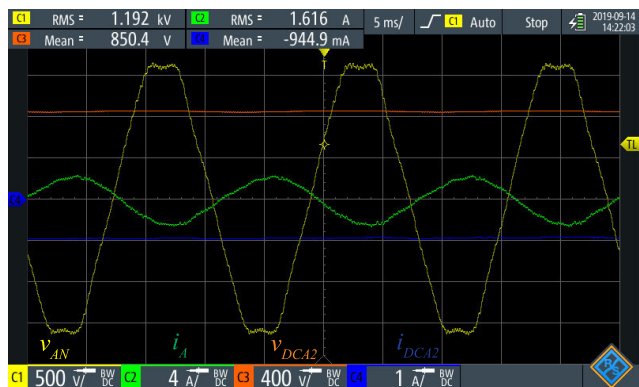

FIGURE 27. Measurements at 14:22, at the 2.42 kV side of the transformer - Converter injecting power into the grid - without harmonic compensation feature.

VI. CONCLUSION

This paper has presented the development aspects of a peak-shaving equipment with energy storage based on lead-acid batteries for 13.8kV power systems. The equipment is based on a multilevel converter whose AC port is connected to the grid using a 2.4kV:13.8kV coupling transformer. The topology of the multilevel converter is the cascaded H-bridge. The isolated DC ports of each of the H-bridges are connected to series arrays of 67 batteries of 12V (resulting in 804V nominal voltage on each bridge). A system for safe connection of the batteries to the DC capacitors of the H-bridges has been presented.

In addition, as the power circuit of the peak-shaving equipment is the same circuit of a shunt active power filter, a feature of damping of harmonic voltage (by the emulation of a harmonic resistance) has been included - without the need for any additional resource. It should be noted that, contrary to the traditional shunt active power filters, the emulated harmonic resistance does not require access to the terminals of the non-linear loads. This characteristic is very appealing to distribution systems, where the non-linear loads may be scattered throughout the line.

The paper has presented the algorithms of both functionalities and experimental results have been collected on a 13.8kV test substation.

APPENDIX A
PHASE LOCKED LOOP - *PLL*

The PLL block of Figure 2 is detailed in Figure 28. It is based on the digital PLL presented by [31]. The phase error Φ between the installation site line-neutral voltage $v_{\Phi N}$ and the unitary sinusoid $sin(\omega_1 t)$ is obtained through the principle of the Coulon oscillator (mathematically explained in [31]). The advantage of this procedure is that no tuning parameters are required, other than the nominal amplitude A of the installation site voltage. A closed loop is used to minimize the phase error Φ.

In order to feedback the estimated unitary angle, a digital procedure, based on look-up table, is employed. Hence, the highlighted block in Figure 28 presents a conversion from the phase error Φ to the index of the look-up table. The phase error Φ corresponds to a number of samples N_S that must be shifted on look-up table. The relation between
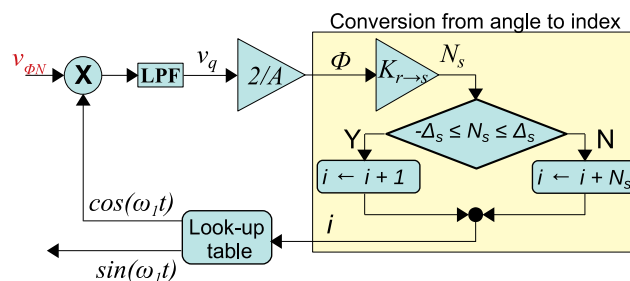

FIGURE 28. Digital PLL based on look-up table.

radians and samples is calculated with (11), where f_{nom} is the nominal frequency of the grid and f_s the sampling frequency of controller.

$$K_{r \to s} = \frac{f_s}{f_{nom} \cdot 2 \cdot \pi}. \tag{11}$$

A hysteresis-band from $-\Delta_S$ to Δ_S is employed in order to tolerate variations on the supply voltage. Whenever the error in terms of number of samples N_S is within the hysteresis-band, then error between the supply voltage $v_{\Phi N}$ and the unitary sinusoid $sin(\omega_1 t)$ is minimal - hence the index i of lookup table needs only to be increment by 1, preparing for the next sample. On the contrary, if the sample error is high, then i is incremented by N_S.

APPENDIX B
PROPORTIONAL PLUS RESONANT CONTROLLER - *PR*
Figure 29 presents the Proportional plus Resonant controller. It is formed by a proportional controller k_p (whose function is to improve transient response) and several resonant controllers (whose function is to minimize steady state errors at each of the resonant frequencies). The continuous frequency domain s for each resonant controller is given by (12).

$$Res_h(s) = \frac{yR_h(s)}{e(s)} = \frac{k_{Rh} \cdot s}{s^2 + \omega_h^2}, \tag{12}$$

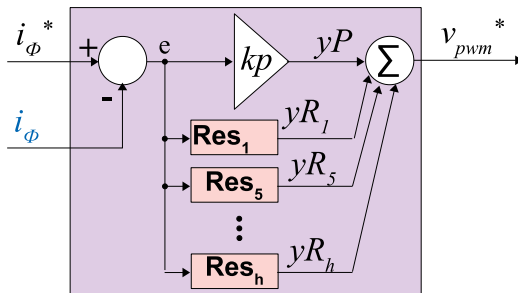where k_{Rh} is the resonant gain at the resonant frequency ω_h.

FIGURE 29. Proportional plus resonant controller.

As this controller is implemented in a Digital Signal Processor, (12) can be discretized with a Trapezoidal/Tustin method [42], resulting in the difference equation (13).

$$v_{pwm}^*(t) = k_P \cdot e(t)$$
$$+ \sum_h b_h \cdot k_{Rh} \cdot [e(t) - e(t-2)]$$
$$- \sum_h [a_{1h} \cdot y_{Rh}(t-1) + a_{2h} \cdot y_{Rh}(t-2)], \tag{13}$$

where a_{1h}, a_{2h} and b_h are parameters defined by (14), dependent on the sampling time $T_s = 1/f_s$ and on the resonant frequency ω_h for each $h = 1, 3, 5, 7, 9$.

$$\begin{cases} a_{0h} = 4/T_s^2 + \omega_h^2 \,; \\ a_{1h} = \left[-8/T_s^2 + 2 \cdot \omega_h^2\right]/a_{0h} \,; \\ a_{2h} = 1 \,; \\ b_i = [2/T_s]/a_{0h}. \end{cases} \tag{14}$$

REFERENCES
[1] W. F. Pickard, "Massive electricity storage for a developed economy of ten billion people," *IEEE Access*, vol. 3, pp. 1392–1407, 2015.
[2] F. Nadeem, S. M. S. Hussain, P. K. Tiwari, A. K. Goswami, and T. S. Ustun, "Comparative review of energy storage systems, their roles, and impacts on future power systems," *IEEE Access*, vol. 7, pp. 4555–4585, 2019.
[3] S. Vazquez, S. M. Lukic, E. Galvan, L. G. Franquelo, and J. M. Carrasco, "Energy storage systems for transport and grid applications," *IEEE Trans. Ind. Electron.*, vol. 57, no. 12, pp. 3881–3895, Dec. 2010.
[4] H. Hesse, M. Schimpe, D. Kucevic, and A. Jossen, "Lithium-ion battery storage for the grid—A review of stationary battery storage system design tailored for applications in modern power grids," *Energies*, vol. 10, no. 12, p. 2107, Dec. 2017.
[5] G. Strbac, "Demand side management: Benefits and challenges," *Energy Policy*, vol. 36, no. 12, pp. 4419–4426, Dec. 2008.
[6] S. J. Chiang, K. T. Chang, and C. Y. Yen, "Residential photovoltaic energy storage system," *IEEE Trans. Ind. Electron.*, vol. 45, no. 3, pp. 385–394, Jun. 1998.
[7] M. A. Acquah, D. Kodaira, and S. Han, "Real-time demand side management algorithm using stochastic optimization," *Energies*, vol. 11, no. 5, p. 1166, May 2018.
[8] D. Connolly, H. Lund, B. V. Mathiesen, and M. Leahy, "A review of computer tools for analysing the integration of renewable energy into various energy systems," *Appl. Energy*, vol. 87, no. 4, pp. 1059–1082, Apr. 2010.
[9] M. Faisal, M. A. Hannan, P. J. Ker, A. Hussain, M. B. Mansor, and F. Blaabjerg, "Review of energy storage system technologies in microgrid applications: Issues and challenges," *IEEE Access*, vol. 6, pp. 35143–35164, 2018.
[10] W. F. Pickard, "The history, present state, and future prospects of underground pumped hydro for massive energy storage," *Proc. IEEE*, vol. 100, no. 2, pp. 473–483, Feb. 2012.
[11] J. Wang, K. Lu, L. Ma, J. Wang, M. Dooner, S. Miao, J. Li, and D. Wang, "Overview of compressed air energy storage and technology development," *Energies*, vol. 10, no. 7, p. 991, Jul. 2017.
[12] M. Hedlund, J. Lundin, J. de Santiago, J. Abrahamsson, and H. Bernhoff, "Flywheel energy storage for automotive applications," *Energies*, vol. 8, no. 10, pp. 10636–10663, Sep. 2015.
[13] D. Akinyele, J. Belikov, and Y. Levron, "Battery storage technologies for electrical applications: Impact in stand-alone photovoltaic systems," *Energies*, vol. 10, no. 11, p. 1760, Nov. 2017.
[14] S. Kharel and B. Shabani, "Hydrogen as a long-term large-scale energy storage solution to support renewables," *Energies*, vol. 11, no. 10, p. 2825, Oct. 2018.
[15] J. Torres, P. Moreno-Torres, G. Navarro, M. Blanco, and M. Lafoz, "Fast energy storage systems comparison in terms of energy efficiency for a specific application," *IEEE Access*, vol. 6, pp. 40656–40672, 2018.
[16] O. Rahman, K. M. Muttaqi, and D. Sutanto, "High temperature superconducting devices and renewable energy resources in future power grids: A case study," *IEEE Trans. Appl. Supercond.*, vol. 29, no. 2, pp. 1–4, Mar. 2019.
[17] C. Rahmann, B. Mac-Clure, V. Vittal, and F. Valencia, "Break-even points of battery energy storage systems for peak shaving applications," *Energies*, vol. 10, no. 7, p. 833, Jun. 2017.
[18] W. C. Sant'Ana, R. B. Gonzatti, G. Lambert-Torres, E. L. Bonaldi, B. S. Torres, P. A. de Oliveira, R. R. Pereira, L. E. Borges-da-Silva, D. Mollica, and J. S. Filho, "Development and 24 hour behavior analysis of a peak-shaving equipment with battery storage," *Energies*, vol. 12, no. 11, p. 2056, May 2019.
[19] W. C. Santana, L. E. B. da Silva, L. E. L. de Oliveira, V. F. da Silva, and G. L. Torres, "13.8 kV series active power filter implementation using a noise-tolerant algorithm," in *Proc. IEEE 35th Annu. Power Electron. Spec. Conf.*, vol. 2, Jun. 2004, pp. 958–964.
[20] C. Guzman, A. Cardenas, and K. Agbossou, "Local estimation of critical and off-peak periods for grid-friendly flexible load management," *IEEE Syst. J.*, vol. 14, no. 3, pp. 4262–4271, Sep. 2020.

[21] J. R. Hammarstron, A. da Rosa Abaide, B. L. Blank, and L. N. F. da Silva, "Analysis of the electricity tariffs in Brazil in light of the current behavior of the consumers," in *Proc. 53rd Int. Universities Power Eng. Conf. (UPEC)*, Sep. 2018, pp. 1–6.

[22] H. Akagi, "New trends in active filters for power conditioning," *IEEE Trans. Ind. Appl.*, vol. 32, no. 6, pp. 1312–1322, Nov./Dec. 1996.

[23] E. Hossain, M. R. Tur, S. Padmanaban, S. Ay, and I. Khan, "Analysis and mitigation of power quality issues in distributed generation systems using custom power devices," *IEEE Access*, vol. 6, pp. 16816–16833, 2018.

[24] F. Z. Peng, "Application issues of active power filters," *IEEE Ind. Appl. Mag.*, vol. 4, no. 5, pp. 21–30, Sep./Oct. 1998.

[25] T.-N. Le, M. Pereira, K. Renz, and G. Vaupel, "Active damping of resonances in power systems," *IEEE Trans. Power Del.*, vol. 9, no. 2, pp. 1001–1008, Apr. 1994.

[26] W. Sant'Ana, R. Gonzatti, G. Lambert-Torres, E. Bonaldi, R. Pereira, L. E. Borges-da-Silva, G. Pinheiro, C. H. Silva, D. Mollica, and J. S. Filho, "Implementation of harmonic propagation damping feature on a storage and grid support equipment (in Portuguese)," *Revista Eletronica de Potencia*, vol. 24, pp. 27–36, Jan./Mar. 2019.

[27] N. Pogaku and T. C. Green, "Harmonic mitigation throughout a distribution system: A distributed-generator-based solution," *IEE Proc.-Gener., Transmiss. Distrib.*, vol. 153, no. 3, pp. 350–358, May 2006.

[28] Y. W. Li and J. He, "Distribution system harmonic compensation methods: An overview of DG-interfacing inverters," *IEEE Ind. Electron. Mag.*, vol. 8, no. 4, pp. 18–31, Dec. 2014.

[29] J. He, Y. W. Li, R. Wang, and C. Zhang, "Analysis and mitigation of resonance propagation in grid-connected and islanding microgrids," *IEEE Trans. Energy Convers.*, vol. 30, no. 1, pp. 70–81, Mar. 2015.

[30] N. Jaalam, N. A. Rahim, A. H. A. Bakar, C. Tan, and A. M. A. Haidar, "A comprehensive review of synchronization methods for grid-connected converters of renewable energy source," *Renew. Sustain. Energy Rev.*, vol. 59, pp. 1471–1481, Jun. 2016.

[31] C. H. da Silva, R. R. Pereira, L. E. B. da Silva, G. Lambert-Torres, B. K. Bose, and S. U. Ahn, "A digital PLL scheme for three-phase system using modified synchronous reference frame," *IEEE Trans. Ind. Electron.*, vol. 57, no. 11, pp. 3814–3821, Nov. 2010.

[32] G. Wang, G. Konstantinou, C. D. Townsend, J. Pou, S. Vazquez, G. D. Demetriades, and V. G. Agelidis, "A review of power electronics for grid connection of utility-scale battery energy storage systems," *IEEE Trans. Sustain. Energy*, vol. 7, no. 4, pp. 1778–1790, Oct. 2016.

[33] P. A. Bettawar and S. R. Punam, "An inclusive review on various multilevel converter topologies for a grid connected photo-voltaic system," *Int. Res. J. Eng. Technol.*, vol. 6, no. 2, pp. 307–311, Feb. 2019.

[34] B. Wu, *High-Power Converters and AC Drives*. Hoboken, NJ, USA: Wiley, 2006.

[35] Y. Li, Y. Wang, and B. Q. Li, "Generalized theory of phase-shifted carrier PWM for cascaded H-bridge converters and modular multilevel converters," *IEEE J. Emerg. Sel. Topics Power Electron.*, vol. 4, no. 2, pp. 589–605, Jun. 2016.

[36] N. Mohan, T. M. Undeland, and W. P. Robbins, *Power Electronics: Converters, Applications and Design*, 2nd ed. Hoboken, NJ, USA: Wiley, 1995.

[37] W. Sant'Ana, R. Gonzatti, B. Guimaraes, G. Lambert-Torres, E. Bonaldi, R. Pereira, L. E. B. da Silva, C. Ferreira, L. de Oliveira, G. Pinheiro, C. H. da Silva, C. Salomon, D. Mollica, and J. S. Filho, "Development of a multilevel converter for power systems applications based on DSP (in Portuguese)," in *Proc. 7th Simposio Brasileiro de Sistemas Eletricos (SBSE)*, Niteroi-RJ, Brazil, May 2018, pp. 1–6.

[38] I. Serban and C. Marinescu, "A look at the role and main topologies of battery energy storage systems for integration in autonomous microgrids," in *Proc. 12th Int. Conf. Optim. Electr. Electron. Equip.*, May 2010, pp. 1186–1191.

[39] W. C. Sant'Ana, R. B. Gonzatti, G. Lambert-Torres, E. L. Bonaldi, P. A. de Oliveira, B. S. Torres, J. G. L. Foster, R. R. Pereira, L. E. Borges-da-Silva, D. Mollica, and J. S. Filho, "Implementation of automatic battery charging temperature compensation on a peak-shaving energy storage equipment," in *Proc. IEEE 15th Brazilian Power Electron. Conf., 5th IEEE Southern Power Electron. Conf. (COBEP/SPEC)*, Dec. 2019, pp. 1–7.

[40] L. Asiminoael, F. Blaabjerg, and S. Hansen, "Detection is key–harmonic detection methods for active power filter applications," *IEEE Ind. Appl. Mag.*, vol. 13, no. 4, pp. 22–33, Jul. 2007.

[41] M. J. Newman, D. N. Zmood, and D. G. Holmes, "Stationary frame harmonic reference generation for active filter systems," *IEEE Trans. Ind. Appl.*, vol. 38, no. 6, pp. 1591–1599, Nov. 2002.

[42] C. L. Phillips and H. T. Nagle, *Digital Control Systems Analysis and Design*, 3rd ed. Upper Saddle River, NJ, USA: Prentice-Hall, 1995.

[43] K. Wada, H. Fujita, and H. Akagi, "Considerations of a shunt active filter based on voltage detection for installation on a long distribution feeder," *IEEE Trans. Ind. Appl.*, vol. 38, no. 4, pp. 1123–1130, Jul. 2002.

[44] W. C. Santana, K. Al-Haddad, and L. E. B. da Silva, "Modeling and active damping of harmonic propagation on electric distribution systems," in *Proc. IEEE Electr. Power Energy Conf. (EPEC)*, Montreal, QC, Canada, Oct. 2009, pp. 1–7.

[45] P. Jintakosonwit, H. Akagi, H. Fujita, and S. Ogasawara, "Implementation and performance of automatic gain adjustment in a shunt-active filter for harmonic damping throughout a power distribution system," *IEEE Trans. Power Electron.*, vol. 17, no. 3, pp. 438–447, May 2002.

[46] T.-L. Lee and S.-H. Hu, "Discrete frequency-tuning active filter to suppress harmonic resonances of closed-loop distribution power systems," *IEEE Trans. Power Electron.*, vol. 26, no. 1, pp. 137–148, Jan. 2011.

[47] W. C. Santana, K. Al-Haddad, and L. E. B. da Silva, "Design procedure for an active resonance damper," in *Proc. 36th Annu. Conf. IEEE Ind. Electron. Soc. (IECON)*, Nov. 2010, pp. 2643–2650.

WILSON C. SANT'ANA (Member, IEEE) received the B.S., M.Sc., and D.Sc. degrees in electrical engineering from the Itajuba Federal University (UNIFEI), Itajuba, Brazil, in 2001, 2004, and 2016, respectively.

Since 2011, he has been a Researcher with Gnarus Institute, Itajuba, Brazil. He has experience with the development of hardware and software for microcontrollers, DSPs, and FPGAs. His research interests include condition-based maintenance, frequency response analysis of electric machinery, power electronics, and control systems. He has written the manuscript and a part of the control software, and performed experiments.

DENIS MOLLICA received the B.S. degree in electrical and electronics engineering and the MBA degree from Taubate University, Taubate, Brazil, in 2000 and 2005, respectively.

Since 1997, he has been with EDP Brasil, where he served in many positions. He is currently the Executive Manager of the Engineering and Systems of the Energy Distribution unity. He has conceptualized the project, provided the material resources, and has written a part of the manuscript.

GERMANO LAMBERT-TORRES (Fellow, IEEE) received the Ph.D. degree in electrical engineering from the Ecole Polytechnique de Montreal, Canada, in 1990.

From 1983 to 2012, he was with the Electrical Engineering Department, Itajuba Federal University (UNIFEI), Itajuba, Brazil, where he was also the Dean of the Research and Graduate Studies, from 2000 to 2004. From 1995 to 1996, he was a Visiting Professor at the University of Waterloo, Waterloo, ON, Canada. Since 2010, he has been the Director of R&D, PS Solucoes, Itajuba. He also serves as a Consultant for many utility companies in Brazil and South America, and has taught numerous IEEE tutorials in the USA, Europe, and Asia. He is the author/editor or coauthor of nine books, more than 30 book chapters, and 50 transactions articles on intelligent systems and nonclassical logic. He has written a part of the manuscript and has conceptualized/supervised the project as a whole.

BRUNO P. B. GUIMARAES received the B.S. degree in electrical engineering from Itajuba Federal University (UNIFEI), Itajuba, Brazil, in 2018, where he is currently pursuing the M.Sc. degree in electrical engineering.

Since 2014, he has been a Research Assistant with the Power Electronics and Industrial Control group (GEPCI), Itajuba. His research interests include power electronics and control systems. He has assembled the hardware and performed the experiments.

GUILHERME G. PINHEIRO received the B.S. degree in automation and control engineering from Uberaba University, Uberaba, Brazil, in 2010, and the M.Sc. degree in electrical engineering from Itajuba Federal University, in 2016, where he is currently pursuing the D.Sc. degree in electrical engineering.

Since 2017, he has been a Research Assistant with the Power Electronics and Industrial Control Group (GEPCI), Itajuba, Brazil. His research interests include power electronics and control systems. He has assembled the hardware and performed part of the experiments.

ERIK L. BONALDI received the B.S., M.Sc., and Ph.D. degrees in electrical engineering from Itajuba Federal University, Itajuba, Brazil, in 1999, 2002, and 2006, respectively.

He is currently the CEO of PS Solutions, Itajuba, Brazil, and also a Research Associate with Gnarus Institute, Itajuba. His research focuses on industrial electronic automation, predictive maintenance, artificial intelligence methodologies, and rough sets classifier. He has conceptualized and supervised the project as a whole.

RONDINELI R. PEREIRA (Member, IEEE) received the B.Sc. degree in computation engineering, and the M.Sc. and D.Sc. degrees in electrical engineering from the Itajuba Federal University, Itajuba, Brazil, in 2007, 2009, and 2011, respectively.

From 2010 to 2012, he was a Professor with the Federal Center of Technological Education of Minas Gerais, Leopoldina, Brazil. Since 2013, he has been a Professor at Itajuba Federal University. His research interests include digital signal processing, adaptive filters, control algorithms for active power filters, harmonics, and power quality. He has written a part of the control software and supervised the experiments.

LUIZ EDUARDO BORGES-DA-SILVA (Senior Member, IEEE) received the B.S. and M.Sc. degrees in electrical engineering from Itajuba Federal University (UNIFEI), Itajuba, Brazil, in 1977 and 1982, respectively, and the Ph.D. degree from the Ecole Polytechnique de Montreal, Montreal, QC, Canada, in 1988.

In 1998, he was a Visiting Professor with The University of Tennessee, Knoxville, TN, USA. He is currently a Professor with the Department of Electronic Engineering, UNIFEI. His research focuses on power electronics, electronic power systems, power converters, and applications of adaptive and intelligent control in industrial problems. He has conceptualized and supervised the project as a whole.

ROBSON BAUWELZ GONZATTI (Member, IEEE) received the B.Sc. degree in automation and control engineering, and the M.Sc. and D.Sc. degrees in electrical engineering from the Itajuba Federal University, Itajuba, Brazil, in 2011, 2012, and 2015, respectively.

Since 2015, he has been a Professor with the Electrical Engineering Institute, UNIFEI. From 2019 to 2020, he was a Visiting Professor with Florida State University, Tallahassee, FL, USA. His research interests include power electronics, active power filters, renewable energy resources, and control systems. He has written a part of the control software and has supervised the experiments.

JOSELINO SANTANA-FILHO received the B.S. degree in electrical engineering from Mogi das Cruzes University, Mogi das Cruzes, Brazil, in 2004, and the M.B.A. degree from the Getulio Vargas Foundation (FGV), Brazil, in 2011.

He is currently with EDP Brasil, as the Project and Studies Engineer of the Technology Development Division. He has experience in the area of electrical engineering, measurement, as well as control and protection. He has conceptualized the project and provided the material resources.

• • •